Biomaterials Advances 174 (2025) 214311



Contents lists available at ScienceDirect

Biomaterials Advances

journal homepage: www.journals.elsevier.com/materials-science-and-engineering-c

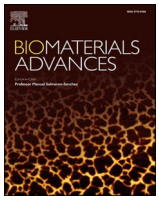



Thin-film NiTi intrasaccular implant with flaps for aneurysm treatments

D. Dengiz [a,*,1], P. Velvaluri [a,1], P. Grotemeyer [a], M.S. Pravdivtseva [b], F. Wodarg [c], J. Watkinson [c], E. Mackensen [a], O. Jansen [c], E. Quandt [a]

[a] Institute for Materials Science, Faculty of Engineering, Kiel University, Germany
[b] Section of Biomedical Imaging (SBMI), Department of Radiology and Neuroradiology, University Hospital Schleswig-Holstein, Kiel University, Germany
[c] Department for Radiology and Neuroradiology, University Hospital Schleswig-Holstein, Kiel University, Germany

ARTICLE INFO

Keywords:
Shape memory alloy
Aneurysm
Intrasaccular implant
Coil-assisting
Flow dynamics

ABSTRACT

Intracranial aneurysms are abnormal, balloon-like formations in the brain blood vessels. They carry a high risk of rupture, which can cause severe complications. Effective aneurysm treatments include reducing blood flow into the aneurysm sac. Coiling is an effective method of occluding the aneurysm sac. However, wide-neck aneurysms are associated with complications because large necks make it difficult to retain the coils securely in the aneurysm sac. This challenge can be overcome by using coil-assisting implants. This additional support avoids the risk of coils migrating into the parent artery avoiding such complications such as ischemic stroke.

This study introduces a novel, coil-assisted implant design with flaps fabricated using micro-electromechanical system (MEMS) technology, which provides a higher degree of freedom in designing and prototyping. The designs contain a stable mechanical backbone with mobile thin flaps that allow secondary delivery of coils into the aneurysm sac. Mechanical tests are conducted to measure radial forces for secure anchoring in the aneurysm sac and compression forces to assess the hammering effect from pulsatile blood flow. Furthermore, the novel implants were tested and compared with a commercial braided implant in in-vitro environment using 3D-printed aneurysm models to understand their flow dynamics and coiling performance by using digital subtraction angiography. The findings showed that backbone/flap designs have greater mechanical stability, which enhances effectiveness compared to braided coil-assisting implants. Moreover, coiling was possible through mobile flaps, highlighting the potential for advancing the treatment of brain aneurysms.

1. Introduction

Brain aneurysms represent a type of weakness in the blood vessel wall that causes localized bulging [1]. This anomaly induces thinning of the aneurysm wall, which, when left untreated, can result in rupture with potentially fatal consequences. Treatment of a brain aneurysm aims to reduce blood flow into the aneurysm sac, promoting clot formation. Many treatment approaches have been established, such as surgical clipping [2] (requiring open craniotomy, where an implant is placed on the aneurysm neck), flow diverter (FD) stents [3](which are placed along the blood vessel), and intrasaccular implants [4](an implant that is placed inside the aneurysm sac). The latter two approaches are minimally invasive, which involve deploying the implants using catheters through transarterial access. FDs are usually preferred for treating sidewall (or lateral) aneurysms. However, they could cause side-branch occlusion when used to treat bifurcating aneurysms. Patients treated with FDs need to receive antiplatelet therapy (APT) for long-term post-surgery [5] to avoid vessel occlusion.

On the other hand, intrasaccular devices can be used in both side-branch and bifurcating aneurysms. They do not cause side-branch occlusion, and in most cases, APT medication is not required after the implantation/treatment. One of the most frequently used implants for intrasaccular treatment is coiling [6], whereby a soft platinum wire is introduced into an aneurysm sac. The coil takes the shape of the aneurysm once it is delivered. Depending on the size of an aneurysm, in many cases, multiple coils are required to fill the complete volume [7]. This treatment may require an additional implant, known as a coil-assisting implant, to help secure and prevent coil migration within the aneurysm [8]. This strategy depends on the aneurysm's shape and geometry, with wide-neck aneurysms being the most common case requiring it. Wide-neck aneurysms have are defined as either having a neck diameter greater than or equal to 4 mm or dimensions of dome-to-neck ratio less

* Corresponding author.
E-mail address: dude@tf.uni-kiel.de (D. Dengiz).
[1] These authors equally contributed to this study.

https://doi.org/10.1016/j.bioadv.2025.214311
Received 7 January 2025; Received in revised form 28 March 2025; Accepted 6 April 2025
Available online 11 April 2025
2772-9508/© 2025 The Authors. Published by Elsevier B.V. This is an open access article under the CC BY-NC license (http://creativecommons.org/licenses/by-nc/4.0/).

than two [9]. Coiling wide-neck aneurysms poses a challenge as coil protrusion can occur and/or embolization with subsequent ischemic stroke might occur. In such cases, an additional coil-assisting device [8] is placed to secure the coils in place and achieve the required packing density [7].

These coil-assisting implants can be classified into two groups: stent-assisted coiling (SAC) and intrasaccular coil-assisting devices. SAC is primarily used to treat side-branch aneurysms and intrasaccular coiling for bifurcating aneurysms. There are many devices [11] on the market for SAC of side-branch aneurysms, most recent/frequently used include NeuroForm Atlas (Stryker, USA) [12], Enterprise (Codman Neuro, USA) [13], and Accero (Acandis GmbH, Germany) [14]. On the other hand, the intrasaccular coil assisting implants are more recent and are increasing rapidly. A few such devices that are currently available include pCONus (Wallaby-Phenox GmbH, Germany) stent-like [15], TriSpan (Boston Scientific, USA) [16], Nautilus [17](Endostream, Israel), Trenza (Stryker, USA) [18], and Neqstent (Stryker, USA) [19]. These devices are intended to be placed at the neck of an aneurysm. These devices have high porosity, meaning they cannot be used as single/stand-alone implants to reduce blood flow sufficiently in the aneurysm sac.

These treatments have shown enhanced stability and good occlusion rates of 94.5 % for Nautilus [17], 80 % for Neqstent [19], and 65.6 % for pCONus [15]. Since all these devices serve as coil-assisting implants, they are deployed without being detached to ensure they remain securely in place. Once they are positioned, the coils are delivered into the aneurysm sac and detached. After the coiling process is completed, the coil-assisting implant is also detached. However, complications of such treatments might include unintended detachment of coil-assisting implants during coil deployment as sometimes there is crosstalk among the electrical detachment systems [20]. Thus, an implant that can hold its place securely on detachment, followed by the placement of coils into the aneurysm, would help to avoid such problems.

There are also other approaches for single implant-based intrasaccular treatments such as Contour (Stryker, USA) [21] and Woven Endo Bridge (WEB, MicroVention Terumo, USA) [22]. These devices do not require or even allow additional coiling because they are designed to reduce blood flow into the aneurysm sac due to low porosity. This approach simplifies treatment, as the implant achieves the desired flow diversion and occlusion on its own without any additional coiling. However, in certain aneurysm geometries, the flow diversion is not sufficient, and stand-alone devices are supplemented with coils to obtain better flow reduction [23]. In such treatments, a second catheter must be inserted to deploy the coil into the aneurysm sac. Here, using the technique known as 'jailing,' the microcatheter enters the aneurysm between the vessel wall and the deployed contour device. Although such a combination yields excellent results, a recent study reported that a complication developed when the Contour became displaced from the neck of the aneurysm and blocked the blood flow within 15 min of being deployed [24]. The physician restored the flow by placing an additional vascular implant to keep the Contour in place.

In the present study, we introduce a novel intrasaccular device fabricated using 2.5D thin-film technology [25]. The implant is envisioned as an intrasaccular implant capable of treating wide-neck bifurcation aneurysms (WNBAs). With this implant, which is designed to provide a good mechanical stability, a microcatheter for coil placement can be inserted either immediately after deploying the implant or at a later point in time, without being attached to its delivery system. We present the design, mechanical characterization, and flow performance of the novel, thin-film implant and compare it to a commercial implant (Neqstent). We conducted mechanical studies to evaluate radial and compression forces. The limited research available on mechanical investigations in the literature highlights the importance of present work to the field. The flow characteristics of Neqstent and our implants were analyzed with digital subtraction angiography (DSA). After determining the initial flow characteristics and placement of the implant onto the neck, the aneurysm sac was filled with coils by a secondary placed intraaneurysmal catheter, and the final flow dynamics were investigated for both devices.

Most aneurysm implants are fabricated from shape memory alloy (SMA) [26]. Owing to their superelastic properties, the implants self-expand upon exiting the catheter [27,28]. Our novel implant is also based on a nitinol binary SMA. Fabricating thin films using microsystem technology not only provides high mechanical stability but also offers significant design freedom [25,29]. Thus, the implant designs can be easily adjusted to be a single implant treatment for an aneurysm, and the aneurysm sac can still be accessed after treatment if necessary. Owing to the wafer-based manufacturing process, additional functions can be integrated into conventional implants, such as increased radiopacity [31] or electrodes for biosensing [32]. Moreover, unique thin films with different layer thicknesses can be fabricated via the so-called 2.5D technology [25]. This process offers great potential for developing next-generation medical implants as each layer can be designed and modified independently to fulfill a specific purpose, such as radiopacity or sensing. Such 2.5D technology-based implants have already shown promising results in fabricating certain patient-specific [33] and origami-based implants [34].

2. Materials and methods

2.1. Fabrication and shape setting of the implants

Structured, free-standing NiTi thin films are fabricated using microsystem technologies such as photolithography, magnetron sputtering, and wet chemical etching (for copper sacrificial layer) as described in detail by Bechtold et al. [31] The designs are patterned on a 4-in. Si wafer by photolithography (Karl Suess MA6, Germany) with two masks, one for flaps and one for backbones. The implants with a 7 μm thickness for the flaps and 35 μm for the backbone are deposited using a Von Ardenne CS730S (Von Ardenne, Germany) cluster magnetron sputter device from a 4-in. binary $TiNi_{46.5}$ (at.%) target (Ingpuls GmbH, Germany). The depositions are done at 2.3×10^{-3} mbar chamber pressure, 20 sccm argon flow, and 150 W DC power, resulting in a deposition rate of 3.3 μm/h for the NiTi. The elemental composition averaged over such a 4-in. Si wafer of these films is measured by energy-dispersive X-ray spectroscopy using a Helios NanoLab 600 scanning electron microscope (SEM, FEI, Germany) equipped with a silicon drift detector (Oxford Instruments, UK). The composition is determined to be $Ti_{49}Ni_{51}$ (at.%) with an error of 0.5 at.% using a binary $Ti_{50.4}Ni_{49.6}$ standard in the area around 30 mm from the center of the wafer. For further experiments, the samples from this region were used in each case to ensure the homogeneity of the composition.

Fig. 1a shows the design scheme and fabricated 2.5D structures of the backbone marked as number 1 (35 μm) and flap (7 μm) types marked as number 2. The microscope image clearly shows the distinction between the backbone and the flap. In Fig. 1b, full flap (FF) and mesh flap (MF) can be seen for the same backbone design. 2D areas of flap and backbone are 28.03 mm^2, for FF and 18.03 mm^2 for MF, they were calculated using the Hatch tool in AutoCAD (Autodesk, USA).

Deposited free-standing NiTi thin films are amorphous and flat. Their shape is set by placing the devices inside a hemispherical titanium fixture. The fixture contains male and female hemispherical parts, where the implant is pushed into the female part and then pressed with the male part. It is constrained with a ring to ensure that the two parts are securely pressed together and remain in place. This fixture is placed into a rapid thermal annealing tool (RTA, CreaTec RTA-6 SY09, Germany) at 700 °C for 300 s to crystallize and shape set the implants simultaneously. After this step, the implants hold their 3D shape, as shown in Fig. 1c. The material properties of crystallized free-standing NiTi thin films were investigated using tensile testing and differential scanning calorimetry measurements and are reported in the Supporting information (SI) section on material properties. SI Fig. S1a represents the tensile curve of

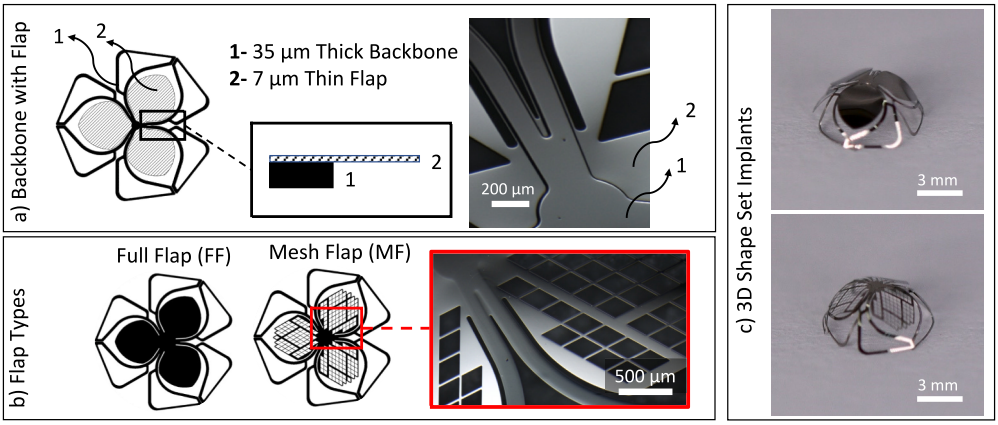

Fig. 1. General concept for the novel flap implants. a) Sketch showing the 2.5D concept of thin flaps with thicker backbone and thin flap and scanning electron microscopic image of the fabricated sample, where number 1 corresponds to the backbone and number 2 to the flap. b) Sketches of the concept of full flap (FF) and meshed flap (MF), with an inset showing an optical microscope image of the mesh structure of the flap. c) Fabricated and 3D shaped set NiTi implants of (FF) (top) and MF (bottom).

NiTi at 37 °C to evaluate the material properties at body temperature, and SI Fig. S1b is the differential scanning calorimetry (DSC) curve to obtain the transformation temperature of NiTi. These results confirm that the austenite transformation temperature is below body temperature, facilitating the superelastic behavior desired for implants [27,28].

2.2. Radial force measurement set-up

The radial force was investigated by placing the implants in a crimping device consisting of 12 individual polyetheretherketone (PEEK) prisms that move collectively to compress and decompress the implant radially while measuring the force [33,35]. All the prisms are connected to a force ring that is further connected to the force sensor (FN 3148-10 N, Disynet GmbH, Germany) and the actuator assembly (M-229.26S and L-306.011100, PI miCos GmbH, Germany). The sensor is supplied with a 10-V input voltage (E3631A Triple output DC, Hewlett Packard, USA) and gives an output of ±2 V, which corresponds to a force of ±10 N accordingly. The data are transmitted to the computer from the sensor using DAQ (S. No: 309B913, NI myDAQ, National Instruments, USA). The complete setup is controlled using the LabVIEW program (V17.0f2 (32-bit), LabVIEW2017, National Instruments, USA).

As the friction between the PEEK prisms scales with the force applied by the implant, a calibration experiment was performed, where a known amount of force was applied and a calibration parameter was evaluated. The calibration details about the correlation between the testing diameter, measured force, and real force can be found in the SI (SI Fig. S2). The measured values were corrected with the calibration parameter and subtracted from the background to obtain the actual force. During the experiments, the setup was placed inside a thermal chamber and maintained at 37 °C (body temperature) throughout the test. A long, thin rod (diameter ~ 1 mm) was glued to the back of the implant to hold it upright during the testing. Each measurement was repeated five times, and the data were plotted with mean and standard deviation.

2.3. Setup for compression resistance characterization

The implants were compressed between two PEEK plates to measure their resistance to compression. The implant was placed on the bottom plate, with a circular indentation of 6.5 mm in diameter and a depth of 1 mm. The indentation kept the implant in place during the testing. The top PEEK plate acted as a stamp and was attached to an assembly of a force sensor (FN 3148-10 N, Disynet GmbH, Germany), linear actuator (L-306.011100, PI miCos GmbH, Germany), and actuator controller (C-663 PI miCos GmbH, Germany). The sensor is supplied with a 10-V input voltage (E3631A Triple output DC, Hewlett Packard, USA) and has an output of ±2 V, corresponding to a force of ±10 N accordingly. The stamp compresses the implant from 0 to 0.4 mm while recording the force. The data are transmitted from the sensor using DAQ (S. No: 309B913, NI myDAQ, National Instruments, USA) to a LabVIEW program (V17.0f2 (32-bit), LabVIEW2017, National Instruments, USA), which also controls the actuator. The complete setup was placed in a thermal chamber at 37 °C during the tests to mimic human body conditions. Each measurement was repeated ten times, and the data were plotted with mean and standard deviation values.

2.4. Microcatheter insertion through flaps

The feasibility of microcatheter insertion through the flap was evaluated by implanting the device at the aneurysm neck and subsequently introducing a microcatheter into the aneurysm. A replica of a wide-necked aneurysm was created using acrylic (SI Fig. S3a). Acrylic was chosen due to its transparency, which provided better illumination for photography and allowed improved control over the positioning of the implant. The model has a 4-mm borehole, representing the aneurysm neck, that is enlarged on one end to the dimensions of a 5.5-mm aneurysm. The top of the aneurysm has a 5 mm opening, allowing for visual inspection of the flap opening with a microcatheter (Trevo Track 21, Stryker, USA). The dimensions and shape of the aneurysm replica are based on information from literature. Nikon D850 with AF-S micro Nikkor 60 lens was used for the photographs and videos of the implants. The photograph sequences were taken while inserting the second catheter, and all the photographs were combined to create a graphics interchange format (GIF) using MATLAB (R2022a, MathWork, USA).

2.5. Aneurysm model design and printing

The flow diversion properties of the implant were evaluated by implanting it into a patient-derived aneurysm model and performing DSA. The artificial aneurysm sac was designed in Fusion 360 (Autodesk, USA) with the following dimensions: height 7.95 mm ± 0.1, neck 3.8 mm ± 0.05, and max. dome 5.76 mm ± 0.6.SI Fig. S3b shows a sketch of the aneurysm design, and SI Fig. S3c the aneurysm combined with the patient-specific vascular tree, as described in previous work by Pravdivtseva et al. [36] The aneurysm was designed as a WNBA with a dome-to-neck ratio of 1.52 ± 0.17, smaller than two [9].

A 3-mm outer layer was added to the inner vascular lumen, and the inner lumen was then subtracted from the resulting structure to create the vessel wall. Next, the flow connectors were added to the endpoints of the vasculature; thus, the aneurysm models could be connected to the flow setup. Three identical aneurysm models were 3D printed using

stereolithography (Clear Photoreactive Resin, Form 3, Formlabs, USA). One model served as a control and remained empty, while implants were deployed in the other two. As the fabricated flap implants do not have a detachment system, the aneurysm models were 3D printed in two parts: the cap and the rest of the aneurysm with arteries (see SI Fig. S3c). Such a design made it possible to deploy the implant into the aneurysm sac from the top. After placing the device, the cap was glued to the rest of the model (see SI Fig. S3d) using UHU Plus quickset (Bolton Adhesives B.V., Netherlands). The empty model and the one used for the commercial implant were also 3D printed in parts to ensure production consistency between the models. Once the glue solidified, the models were tested for leakage with a centrifugal flow pump (Ismaltec MCP Standard, Cole Parmer, USA).

2.6. Flow setup

The 3D-printed aneurysm models were connected to the close-cycle flow setup. The flow setup included: a centrifugal pump (Ismaltec MCP Standard), a reservoir filled with saline solution 0.9 % (B. Braun Melsungen AG, Germany), clamp-on transonic flow sensor (ME8PXL-M12, Transonic System Inc., USA), and silicone tubing for the connection (inner diameter of 6 mm). Saline solution with a mean flow rate of 190 ml/min was pumped through the system to mimic in vivo blood flow observed in the basilar artery [37], with flow measurements taken at the model's inlet. All measurements were carried out at room temperature (22 ± 3 °C).

2.7. Implantation

A 7-mm Neqstent was implanted into a 3D-printed aneurysm (the cap and the rest of the aneurysm model are glued prior to deployment) model under fluoroscopy (Allura Xper FD, Philips, The Netherlands) by a neuroradiologist with more than 10 years of interventional experience. For implantation, an intermediate catheter was employed (Sofia ex 0.058″, Microvention Terumo, USA), and a microcatheter (Trevo Pro18, Stryker, USA) navigated into the center of the sac of the aneurysm model. Then, the implant was placed at the neck of the aneurysm. The coil was implanted before detaching Neqstent, as recommended by the manufacturer. Prior to coiling, an additional microcatheter (Stryker Trevo Pro14, USA) was inserted into the intermediate catheter, and a guidewire (Trasend 0.010 guidewire, Boston Scientific, USA) was employed to ensure proper placement of the microcatheter needed to place the coil within the aneurysm sac. After confirming the correct placement, the guidewire was pulled out, and coils were inserted. In total 4 coils were used: Stryker Target 360 Standard, USA (5 mm × 20 cm), Stryker Target 360 Soft, USA (4 mm × 15 cm), Stryker Target 360 Standard, USA (3 mm × 8 cm), and Stryker Target 360 Soft, USA (3 mm × 10 cm). Then, Neqstent was detached from the catheter electrolytically.

The thin-film flap implant has no detachment system; therefore, it was placed into the aneurysm from the top, and the cap glued. The positioning of the implant was then checked using fluoroscopy (Allura Xper FD, Philips, The Netherlands). For implantation of the coils, the same brands of intermediate catheter, guidewire, and microcatheter were used as for Neqstent. After the microcatheter was placed into the aneurysm sac, a total of five coils were implanted: Stryker Target 360 Standard, USA (5 mm × 20 cm), Stryker Target 360 Soft, USA (4 mm × 15 cm), Stryker Target 360 Soft, USA (3 mm × 10 cm), Stryker Target Helical Ultra, USA (3 mm × 8 cm), and Stryker Target Helical Ultra, USA (3 mm × 8 cm). SI Fig. S3e shows a DSA image of the coil implanted through the full flap in the model.

2.8. Digital subtraction angiography

To assess the devices' flow-modulation efficiency, the angiographic contrast agent washout from the aneurysm sac was recorded before and after implanting the device using 2D DSA (Azurion, Philips, The Netherlands). The following sections describe the DSA data acquisition, post-processing, and washout curves derived from the DSA data obtained.

2.9. DSA data acquisition

The time resolution for DSA was 0.083 s (12 fps) and performed using an injection pump (Accutron HP-D, Medtron, Germany), which delivered 2 ml of contrast agent (Isovist-300, Schering Gmbh, Germany) over 0.1 s.

A 2D DSA projection of the aneurysm dome without overlapping side branches was selected for the analysis. The intermediate catheter's distal tip was positioned about 10 cm from the neck of the aneurysm to facilitate a homogeneous mixing of the contrast and saline solution before reaching the aneurysm. DSA was repeated five times for each model with and without devices.

2.10. DSA data post-processing

An image with maximal contrast filling in the aneurysm sac was selected from each dataset. This image served as a raw map to create two regions of interest (ROIs): one for the aneurysm (Fig. 4a, red polyline around aneurysm sac) and one for the background (Fig. 4a, blue square). The aneurysm ROI was drawn manually (MATLAB R2022a, MathWork, USA), while the background ROI was automatically generated as a square (100 × 100 px), and the position was then adjusted to ensure that it did not overlap with the vasculature. These ROIs were created for a single image and then applied to all time frames and five experimental repetitions, as the positioning remained consistent.

The average gray scale value within each ROI was calculated for each time frame to generate a time-density curve (TDC). The TDC of the aneurysm ROI was subtracted from the TDC of the background ROI (MATLAB R2022a, MathWork, USA), and the resulting washout curve was normalized to a maximum amplitude of 1. TDC curves are used to calculate peak intensity time (P_t), mean transit time (MTT), wash-in slope (WIS), and washout slope (WOS) [38,39]. P_t is calculated as the contrast agent arrival time (CAAt) into the aneurysm sac subtracted from the time of maximum intensity. CAAt describes the time when the contrast agent arrives in the ROI, enhancing the signal. MTT is calculated by subtracting CAAt from the time at which the signal reaches half of the peak intensity value during the washout phase. MTT estimates the average time that the contrast agent stays within the ROI. It is calculated as CAAt subtracted from half of peak intensity time on washout curve [40]. The slope from the CAAt to the P_t represents the WIS, while the slope from P_t to the full washout point represents the WOS. WIS shows how rapidly the contrast agent enters the aneurysm sac, and WOS shows how slowly it leaves the aneurysm sac. SI Fig. S4 illustrates schematically how these values are obtained.

2.11. DSA washout time based on the fit

The washout curves were fitted using Eq. (1), which models the convective washout process via a least-squares minimization method [38,39,41].

$$model - c(t) = \rho_c \int_0^t \frac{1}{\delta\sqrt{2\pi}} e^{\frac{-(\eta-\mu)^2}{2\delta^2}} \times \frac{1}{\tau_c} e^{\frac{-t-\eta}{\tau_c}} d\eta \quad (1)$$

Here, ρ_c and ρ_d represent the amplitudes; τ_{conv} is the convective time constant; and μ and δ describe the contrast injection profile. Each parameter was determined with a confidence interval (σ), and accuracy was defined as the relative error σ/*parameter*. More details are provided in [38,39,41].

Spearman's rank correlation coefficient (rho) and the root-mean-square deviation (RMSD) between the experimental washout curve

and fitted models were calculated to determine the goodness of fit.

When the goodness of fit was established, τ_{conv}, values were extracted based on Eq. (1) for comparison for each control (empty), Neqstent, and full-flap implanted model.

3. Results

3.1. Mechanical investigation

Radial forces and compression tests were used to analyze implant stability for Neqstent, full flap (FF), and mesh flap (MF) thin film implants. Fig. 2 shows the mechanical investigations of the FF, MF, and Neqstent devices. The data show mean values and standard deviation (lighter shade of the color used) for ten cycles (compression) and five cycles (radial force) measurements at body temperature (37 °C).

Fig. 2a demonstrates the radial force of all the devices upon expanding from 3 mm to 6.5 mm; the region of interest marked in blue is from 4 mm to 5.5 mm. This region corresponds to the Neqstent manufacturer's recommended diameter for working range for its size. The 7 mm Neqstent would anchor in this region once it is placed into an aneurysm with a neck size of 3–5 mm [19,42]. The thin-film implant was designed to fit an aneurysm similar to the one a 7 mm Neqstent would fit, intended for an aneurysm neck of 3–5 mm. In the region of interest at 4 mm, the Neqstent has the highest force (113 mN), followed by FF (77 mN) and MF (72 mN). However, towards the middle of the interested region at a 4.7 mm diameter, the behavior of the Neqstent changes, and the radial force decreases below the MF. From 4.7 mm to 5.5 mm, the behavior is unchanged, with FF having the highest force for a given diameter, followed by MF, and then Neqstent. At a diameter of 5.5 mm, the radial force of Neqstent is almost zero, while FF has a radial force of 16 mN, and MF corresponds to 13 mN.

Fig. 2b shows the compression force for all the devices, which is higher for both the FF and MF than for the Neqstent. At maximum compression of 0.3 mm, both the thin-film devices (FF and MF) show similar forces (~0.15–0.2 N), with very small hysteresis between the forward and the reverse curves. Neqstent, in contrast, has a low compression force, about seven times smaller at 0.3-mm compression. For the thin-film devices, irrespective of their flap configurations, compression force is consistently above that for Neqstent throughout the measurement.

3.2. Microcatheter insertion through flaps

One of the main aims of this study was to investigate the technical feasibility of inserting a microcatheter into the aneurysm sac after placing the device over the aneurysm neck. To visualize this, the devices were placed inside a model aneurysm, and a microcatheter was inserted. A series of images show the device before (Fig. 3a), during (Fig. 3b), and after (Fig. 3c) placing the microcatheter. The GIFs created with these images can be found as SI Video V1a and b for FF and MF, respectively. Both the FF and MF allow the insertion of the microcatheter and the device holds its position during and after the insertion. This strongly supports the hypothesis for the design that the novel thin flaps allow passage of the catheter to the intrasaccular volume for coiling after the device has been placed. The stability of the device while inserting the catheter also suggests that the radial force exerted by the device is strong enough to hold its position. These results also show that the implant has good mobility on the flaps, and owing to the material superelasticity, the flaps can fully recover; as seen in Fig. 3c, the flaps returned to their initial position without permanent deformation.

3.3. Flow investigation

Flow modulation efficiency was assessed for the FF device using DSA and compared to the performance of Neqstent. The washout curves were based on the TDC calculated in the aneurysm and background ROIs, red polygon, and blue square, respectively (Fig. 4a). The resulting experimental washout curves (blue) and fit curves (red) are shown in Fig. 4b, c, and d for the empty 3D-printed aneurysm model, with Neqstent and the FF implant before coiling, respectively.

The contrast agent was almost fully washed out in 12 s (signal intensity = 0.092 ± 0.03) from the empty aneurysm sac, while it remained in the aneurysm model with the commercial (signal intensity =0.153 ± 0.4) and FF (signal intensity = 0.195 ± 0.04) implants. Overall, the commercial and flap implants showed similar signal intensities at 12 s. However, for the FF implant the standard deviation between repetitions was smaller, indicating a higher flow stability.

Both the commercial and FF implants broadened the washout curves compared to the control empty model. The MTTs are 4.9 ± 0.4, 6.4 ± 1.1, and 6.7 ± 0.1 for empty, Neqstent, and FF implants, respectively. The commercial implant increased MTT by 30.6 %, and the FF by 36.7 %. This increase is likely due to the delayed entry of the contrast agent into the aneurysm and a later start of the washout process caused by implants.

The curve slope characteristics were analyzed using WIS and WOS. WIS, which indicates how quickly contrast enters the aneurysm sac, decreased by 37.2 % for the commercial implant and by 55.1 % for the FF implant compared to the empty model. Whereas WOS, which measures how fast the contrast agent leaves the aneurysm, showed no difference between the models, with values of 0.93 ± 0.01, 0.92–0.02, and 0.94 + 0.01 for the empty, commercial, and FF models, respectively.

In addition, the washout time (τ_{conv}), calculated using a

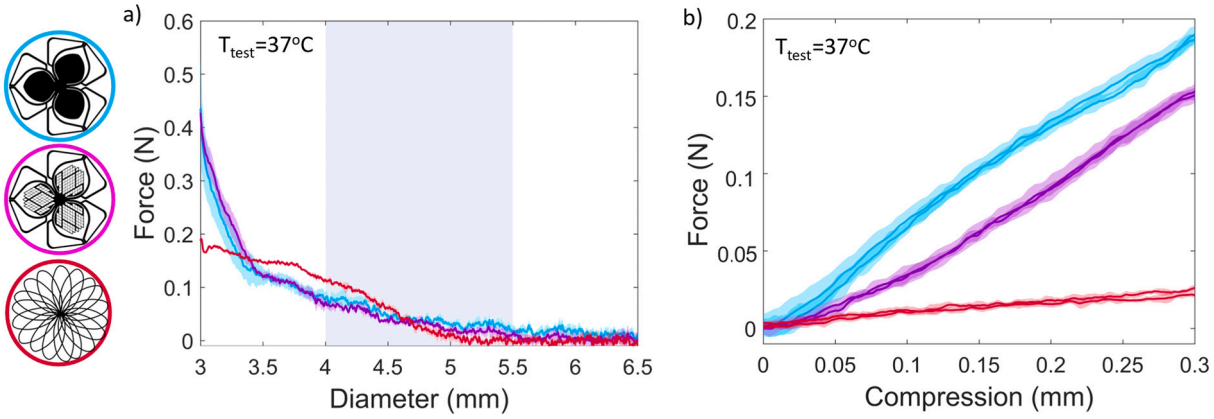

Fig. 2. Mechanical investigations of the full-flap (FF, purple), mesh-flap (MF, blue), and Neqstent (red) devices at body temperature (37 °C). a) The radial force of all the devices upon expanding from 3 mm to 6.5 mm; the range of recommended aneurysm dimensions for implant usage, highlighted with a light blue background, range from 4 mm to 5.5 mm. (b) The compression force for all the devices.

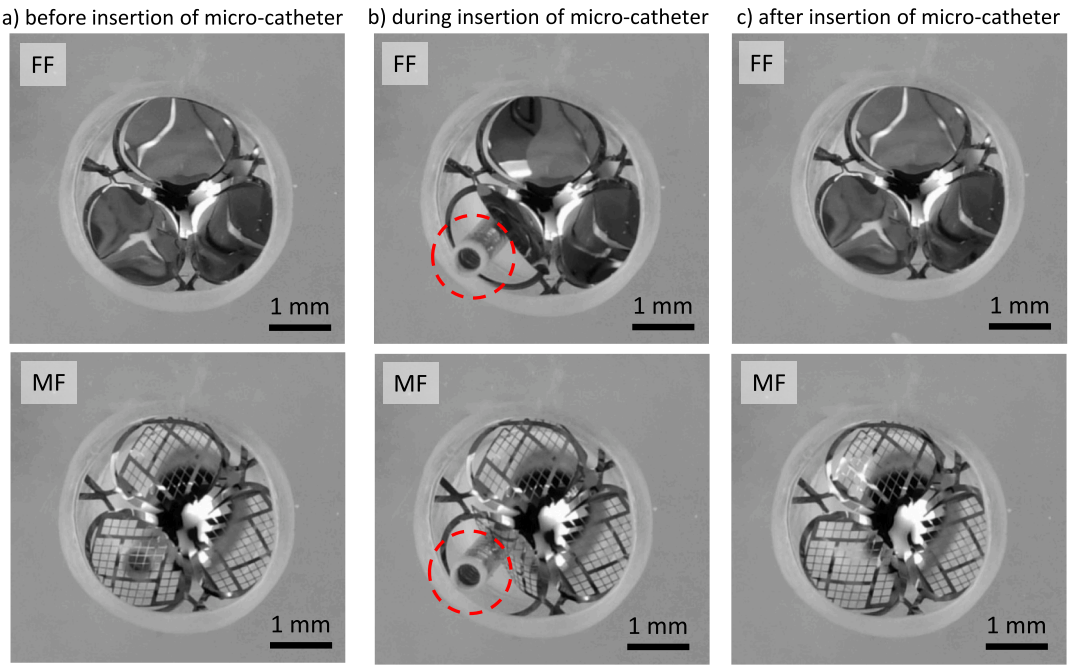

Fig. 3. Image series of a microcatheter insertion for full-flap (FF, top row) and mesh-flap (MF) implant (bottom row). Implants placed on the neck of the artificial aneurysm a) before insertion as the initial position, b) during insertion, the implants retain the initial position only flaps are opened, and c) after retracting the microcatheter where the implants still retain the initial position, and flaps go back to the closed position.

mathematical fit [38,39,41,44], was higher for the models with implants (5.2 ± 1.4 for commercial and 5.1 ± 0.4 for FF) than for the empty model (4.5 ± 0.5). Low RMSD, 0.3 for the empty model, 0.5 for Neqstent, and 0.4 for FF, values and high correlation coefficients (0.97 for all three) were found between experimental data and the fit, indicating the fit accuracy. All the results are summarized in Table 1 and shown as a bar graph in Fig. 4e.

3.4. Coiling

Both the commercial implant and FF were successfully placed over the neck of the aneurysm, showing good apposition to the aneurysm wall (Fig. 5a and e).

After recording the washout curves for both implants, coiling was performed. The microcatheter was navigated through the implants into the aneurysm sac, monitoring its position via biplanar fluoroscopy (Fig. 5b and f) to ensure it was properly traversing the implant rather than entering from the side (jailing). DSA projections were recorded between coil insertions to check the packing density of the aneurysm sac (Fig. 5c and g).

Finally, the contrast agent was injected (Fig. 5d and h) to evaluate the flow into the aneurysm sac. Both implants were successfully coiled, preventing any contrast agent from entering the aneurysm sac.

4. Discussion

In the mechanical investigation of radial force, we found that the FF has a slightly higher radial force, with a mean of 10.4 mN and a standard deviation of 6.6 mN, than the MF in the region of interest between 4 mm and 5.5 mm (SI Fig. S5). Although the area of FF is around 1.5 times greater than the area of MF (28.03 mm^2 for FF and 18.03 mm^2 for MF), the maximum difference in radial force between them in this region is 20.9 mN. This difference can be attributed to the reduced thickness of the flap, which is a minor contributor to the radial force. A major part of the radial force originates from the backbone, which has the same 2D area and thickness. In contrast, the Neqstent radial force varies considerably. At a 4 mm diameter, its radial force is 46 % higher than that of the FF device. At 4.7 mm, the radial forces of all devices are approximately the same (32–40 mN). At the end of the range, at 5.5 mm, the radial force of the Neqstent approaches zero, while that of the FF is 16 mN.

Radial force constitutes an essential parameter for assessing the reaction force as a device expands. Too high a force could either damage the aneurysm tissue or it could protrude out from the aneurysm and block blood flow in the parent vessel [45]. On the other hand, low force would mean that the device can migrate from its optimal position and cause unnecessary complications, such as aneurysm regrowth. Recently, a study using the Contour device showed complete displacement of the device into the aneurysm at an 18-month follow-up examination [46]. The authors attribute this to the blood hammer effect on the implant and a reduction in radial force. This could be due to aneurysm growth post-treatment induced by medication or the patient's lifestyle. Thus, radial force in intrasaccular implants plays a crucial role in securing its position. Another point to consider is that when the radial force is weak, there is a potential risk of the device inverting over time due to the water hammer effect [47,48].

When compared to the other implants, the laser-cut stents have a very high nominal radial force (100–200 mN/mm) [49] compared to the braided stents (2–10 mN/mm) [50], measured at 85 % of the free diameter. The radial force of stents fabricated with thin-film technology at the deployable diameters is similar to that of the braided devices [33]. The difference in radial force is attributed to the material properties that are associated with the varying manufacturing processes such as tube drawing (laser-cut) [51], wire braiding [51], and thin-film technology [52]. In addition, braids might lead to instability and lower radial forces as a result of wire slippage compared to the other methods that provide interconnected structures. Nevertheless, this slippage gives the implant flexibility and thus helps adapt itself to the shape of arteries/aneurysms [53,54].

Although numerous studies focus on the radial force in stents, the literature on this parameter in braided intrasaccular devices is limited. Mine et al. used the finite element method to estimate the radial force in WEB devices [55], reporting regions of constant radial force for certain designs, although they did not provide absolute values for comparison.

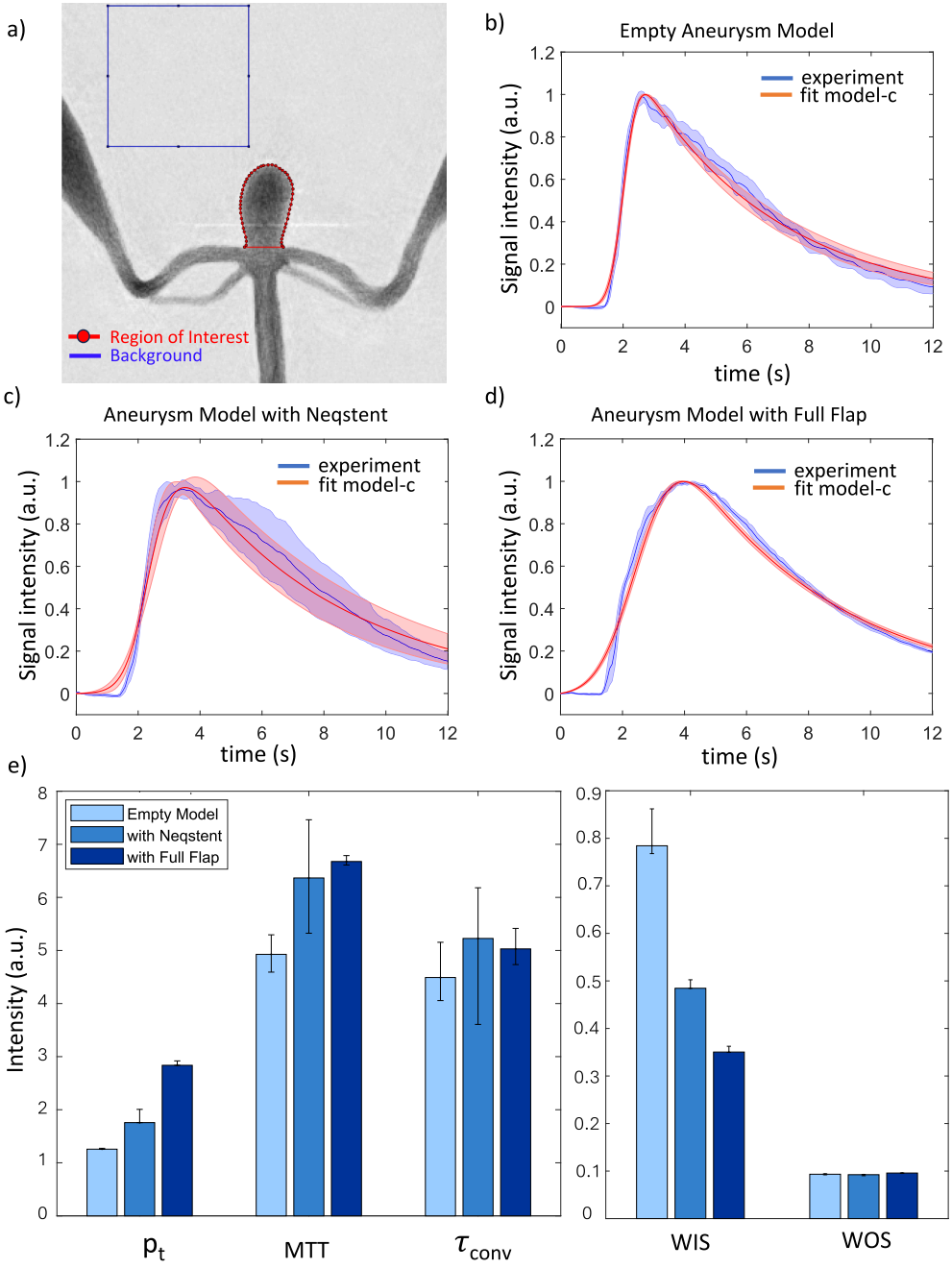

Fig. 4. a) Mask for the aneurysm (red polyline) and the background (blue square) used for washout calculations and these calculated curves for b) empty aneurysm model without any implant, c) aneurysm model with Neqstent, d) aneurysm model with full-flap implant. Lighter shades are standard deviations from five measurements. P_t, peak intensity time; MTT, mean transit time; τ_{conv}, washout time; WIS, wash-in slope; WOS, washout slope.

Table 1
Parameters obtained from the DSA measurements. P_t, peak intensity time; MTT, mean transit time; τ_{conv}, washout time; WIS, wash-in slope; WOS, washout slope.

	P_t	MTT	T_{conv}	WIS	WOS
Empty	1.3 + 0.02	4.9 ± 0.4	4.5 ± 0.5	0.78 ± 0.02	0.93 ± 0.01
Neqstent	1.7 + 0.3	6.4 ± 1.1	5.2 ± 1.4	0.49 + 0.02	0.92–0.02
Full flap	2.8 + 0.08	6.7 ± 0.1	5.1 ± 0.4	0.35 ± 0.02	0.94 + 0.01

More recent research measured the radial force of WEB devices by compressing them between two plates [56], showing how radial force variation affects device selection for a given aneurysm. Therefore, a common guideline is to select a device with a diameter 1 mm larger than the aneurysm width [45]. The authors found that larger devices (7 mm in diameter) exhibit lower radial forces at 1 mm compression than smaller ones (4.5 mm in diameter), recommending a 2 mm compression for devices with larger diameters. Based on the provided data and discussion, it can be inferred that a radial force of 8.8–18 mN is necessary for stable device placement [56]. In the present study, the Neqstent, FF, and MF devices demonstrate radial forces of 0, 16, and 13 mN, respectively, at 1 mm compression. At 2 mm compression, these devices exhibit radial forces of 60, 47, and 36 mN, respectively (Fig. 2a). This suggests that the Neqstent cannot be used at the typical 1 mm compression recommended for WEB devices; instead, a higher compression of 1.5–2 mm is needed. In contrast, the thin-film implants FF and MF show higher radial forces at 1 mm compression, which is within the acceptable force range for WEB devices, allowing their use at

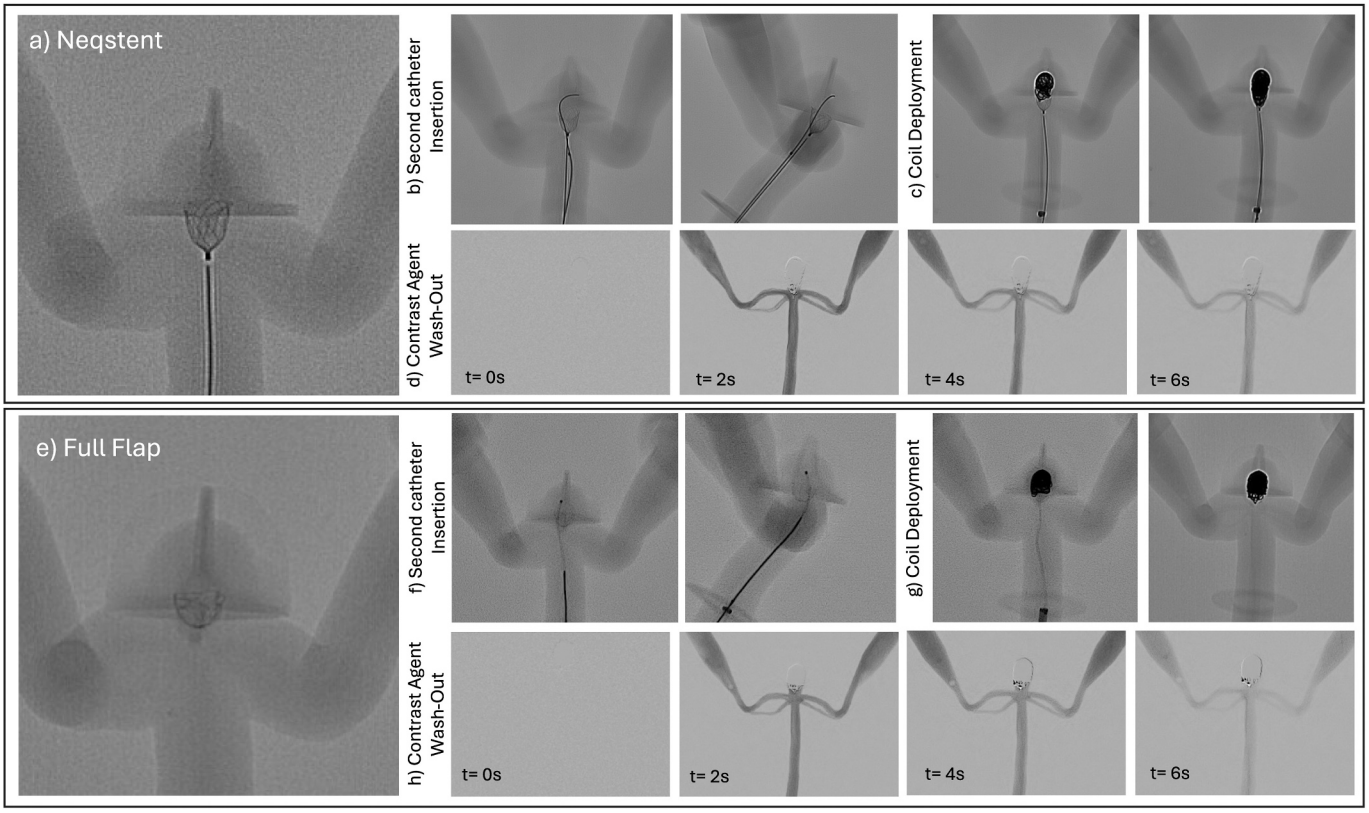

Fig. 5. a) Digital subtraction angiography (DSA) images to prove the correct placement of Neqstent, b) biplanar DSA images of aneurysm model with Neqstent, left front view and right view for checking the microcatheter insertion position, c) DSA images of aneurysm model with Neqstent after coil deployment, d) dynamic DSA series showing the wash-in and -out of contrast agent into the aneurysm model with Neqstent to check coil density, e) DSA images of aneurysm model with full-flap (FF) implant for placement check, f) biplanar DSA images of aneurysm model with FF implant, left front view and right view, for checking the microcatheter insertion position, g) DSA images of aneurysm model with FF implant after coil placement, h) dynamic DSA series showing wash-in and -out of contrast agent into the coiled aneurysm model with FF implant to check coil density.

this 1 mm compression level.

The compression force is the resistance the device exerts when subjected to compression load. The higher the force is, the higher the resistance/stability of the device when an external force is acting on the device. After placing the implants in vivo, constant pulsatile blood flow is acting on the device, this is also known as the water hammer effect, and clinical data have shown that the devices can deform over time due to such loading. By using the compression setup, we could investigate the resistance of the device under similar conditions.

In the compression force measurements, both the FF and the MF have similar amounts of force, irrespective of varying 2D area. This can also be attributed to the reduced thickness of the flap's structure, which makes a minor contribution to the compression force, and a thick backbone with the same 2D area, thickness being a major contribution. The thin-film devices (FF and MF) have a compression force that is about seven times higher than that of the Neqstent device while having the same radial force. Higher compression force could be considered beneficial as it may help anchor the device in a stable position. This is important as, while inserting the secondary catheter, the catheter might hit the backbone instead of the flap. In such cases, the device should be stable enough to prevent migration of the device into the aneurysm. However, there is a significant lack of research on the optimal implant compression force. Therefore, more intrasaccular implants need to be tested and combined with long-term clinical data to gain a more detailed understanding.

An advantage of thin-film technology is that one can control the 2D design and thickness, which can directly reflect on the force that the device (FF and MF) exhibits. If required, the device can be optimized to have a lower or higher compression force by modifying the thickness of the backbone.

Evaluating the mechanical stability of implants is crucial to ensure they can withstand the physiological forces without deforming or failing, which is essential for long-term patient safety. However, understanding the flow behavior of these implants is equally important as flow dynamics show effectively that the implant can regulate blood flow and prevent aneurysm growth or rupture.

One fundamental parameter for assessing treatment efficiency is flow velocity reduction. One approach to assessing flow characteristics is to monitor contrast agent stasis with DSA. Prolonged contrast stasis immediately after implanting a device is considered a predictive marker for aneurysm occlusion [38]. Stasis can be evaluated using contrast washout curves and metrics that describe how quickly contrast enters (WIS), exits (WOS), or remains (MTT) in the aneurysm. As an in vivo modality, DSA evaluates implant placement without any assumptions about virtual positioning [36]. Additionally, it does not require transparency as for particle image velocimetry [57] and flow modulation devices do not create image artifacts at the aneurysm neck as in 4D MRI [58,59], making DSA a good tool for this purpose [36].

Therefore, in this study, we evaluated the washout curves measured with DSA to assess the flow-diversion efficiency of the FF implant compared to the commercial implant and the preimplantation state. For deploying the device, 3D-printed patient-derived aneurysm models were used. These models replicated and modified from patient-specific vascular geometries and flow patterns [60]. Moreover, the velocity reduction measured in in vitro models is similar to those calculated with Computational Fluid Dynamics (CFD) and corresponds with those for successful treatment outcomes [61].

The washout curves (experimental and fit) analyzed to understand

the flow dynamics of both implants and the empty model were used as controls. These parameters are crucial to understanding how the implant contributes to reducing blood flow.

To ensure reproducibility and reduce operator variability, we used a calibrated injection pump to control the contrast agent injection, avoiding issues such as inertia from the contrast reservoir that were reported previously [38]. This allowed for consistent CAAt values and minimized standard deviations between consecutive measurements. CAAt values were 1.44 s for the empty model and Neqstent, 1.33 s for the FF. They were in a similar range for these measurements, meaning the injection with a syringe pump was done systematically in a similar manner.

Sadasivan et al. showed that the parameters obtained from washout curves such as P_t and MTT should increase with better flow diversion, WIS should decrease with better flow diversion, indicating slower wash-in, and WOS should increase with better flow diversion, indicating slower washout [38,39]. Both implants induced changes in washout curves, resulting in higher P_t and MTT, lower WIS, and higher τconv values, indicating a flow diversion effect. FF implants showed a higher increase in MTT at 55.8 % than Neqstent at 33.4 %. WIS values also decreased for implants with a rate of 38.5 % and 55.6 % for Neqstent and FF, respectively. FF outperformed Neqstent in flow diversion.

WOS values did not change overall for the two implants. Although. τ_{conv} and WOS characterize the same thing. τ_{conv} might be a more sophisticated measurement able to depict even subtle changes in the contrast washout dynamics. τ_{conv} increased with better flow diversion, indicating a delayed washout. τ_{conv} showed higher values for both implants compared to empty control models. FF increased by 13.3 % and Neqstent by 15.6 %. The two implants showed similar behavior in flow dynamics, indicating comparable performance.

In this study, we initially evaluated implant performance without coiling to understand the flow dynamics of the current designs. This flow analysis is essential for identifying further design improvements and potentially creating a stand-alone implant capable for coil deployment later if the flow reduction in the aneurysm sac is insufficient, immediately after implantation or post-surgery. Overall, the flow diversion observed was moderate and less substantial than reported for stand-alone implants such as Contour, where the washout time increased after implantation in the range of 1.5 s to 11 s [36]. It is important to note that both the FF and commercial implants are coil-assisted and, thus, a moderate flow diversion is expected compared to stand-alone devices such as Contour. Despite this fact, the moderate flow diversion and contrast stasis observed for both implants could be beneficial for treating acutely ruptured aneurysms, first securing the neck and then deploying the coils. It is worth mentioning that, in the current state, the implants may not be suitable for treating extremely wide neck aneurysms, as the implants do not generate the required radial force to anchor the device securely.

Furthermore, with proper design considerations, the thin-film implants could be used as stand-alone devices (not demonstrated in this work) that potentially allow the physician to access the aneurysm (via flaps) for coiling during a follow-up treatment if the required occlusion is not achieved. In comparison, such a treatment is challenging with braided stand-alone devices such as Contour. During a follow-up, if Contour does not achieve the required occlusion, there is little to no chance of coiling the aneurysm without displacing the Contour. In such cases, additional intraluminal devices, such as stents for assisted coiling or flow diverters, are required to achieve the necessary occlusion [62].

5. Conclusion

In this study, our novel, thin film-based nitinol implant fabricated using microsystem technology provided high mechanical stability and showed comparatively good flow dynamics for use as a coil-assisting implant. The position of the thin-film implant remained stable and did not migrate during microcatheter insertions for coil deployment. Such a novel device would offer great flexibility in treating complex aneurysm geometries, particularly WNBAs, which are among the most challenging to treat. Further studies are required to understand better implant performance, including expanded sampling in mechanical studies and investigating the impact of radial forces on arterial/aneurysm tissue.

Regardless of the various advancements, there is a need for a hybrid intrasaccular device that can function both as a single and/or as a coil-assisting implant. The availability of such a device would constitute a great technological innovation that could combine the ease of use and safety of a single implant and the enhanced occlusion of coil-assisted devices. The current implant designs can be improved to be able to use them as stand-alone implants, and more specifically, capable of allowing insertion of the microcatheter directly after implantation for coiling or at a later point when the physician requires coiling.

Supplementary data to this article can be found online at https://doi.org/10.1016/j.bioadv.2025.214311.

CRediT authorship contribution statement

D. Dengiz: Writing – original draft, Visualization, Methodology, Investigation, Formal analysis, Data curation, Conceptualization. **P. Velvaluri:** Writing – original draft, Visualization, Methodology, Investigation, Formal analysis, Data curation. **P. Grotemeyer:** Writing – review & editing, Software, Methodology, Formal analysis, Data curation, Conceptualization. **M.S. Pravdivtseva:** Writing – review & editing, Validation, Methodology, Data curation. **F. Wodarg:** Writing – review & editing, Validation, Data curation. **J. Watkinson:** Writing – review & editing, Validation, Data curation. **E. Mackensen:** Writing – review & editing, Validation, Software, Data curation. **O. Jansen:** Writing – review & editing, Validation, Supervision, Resources, Project administration, Funding acquisition, Conceptualization. **E. Quandt:** Writing – review & editing, Validation, Supervision, Resources, Project administration, Funding acquisition, Conceptualization.

Declaration of competing interest

The authors declare the following financial interests/personal relationships which may be considered as potential competing interests: Duygu Dengiz reports financial support was provided by DFG, Research Training Group 2154 Materials for Brain (Project number 270394294). Mariya S. Pravdivtseva reports financial support was provided by Intramural Research Funding from the Faculty of Medicine at Kiel. Mariya S. Pravdivtseva reports financial support was provided by Bruhn Foundation. Olav Jansen reports a relationship with ee from Philiconsultant for Acandis, Stryker, RH-DT that includes: consulting or advisory. Olav Jansen reports a relationship with Guerbet, Rapid AI, Boehringer, Bayer, mRAY, Lilly that includes: speaking and lecture fees. Fritz Wodarg reports a relationship with from Balt International SAS, Acandis GmbH, Stryker Corporation, Terumo Neuro, Johnson & Johnson and Phenox that includes: consulting or advisory and speaking and lecture fees. Duygu Dengiz, Prasanth Velvaluri, Eckhard Quandt, Olav Jansen has patent pending to Kiel University.

Acknowledgement

This work was supported by DFG, Research Training Group 2154 Materials for Brain (Project number 270394294), Intramural Research Funding from the Faculty of Medicine at Kiel and Bruhn Foundation. We thank Isil Winkler for discussions during the initial stages of this work. We acknowledge support by Kiel University and the Medical Faculty for supporting the 3D lab of SBMI. Graphical abstract is prepared with Biorender.com.

Data availability

Data will be made available on request.

References

[1] W.I. Schievink, Intracranial aneurysms, N. Engl. J. Med. 336 (1) (1997) 28–40, https://doi.org/10.1056/NEJM199701023360106.

[2] T.E. Darsaut, J.M. Findlay, E. Magro, et al., Surgical clipping or endovascular coiling for unruptured intracranial aneurysms: a pragmatic randomised trial, J. Neurol. Neurosurg. Psychiatry 88 (8) (2017) 663–668, https://doi.org/10.1136/JNNP-2016-315433.

[3] Y.J. Alderazi, D. Shastri, T. Kass-Hout, C.J. Prestigiacomo, C.D. Gandhi, Flow diverters for intracranial aneurysms, Stroke Res Treat. 2014 (1) (2014) 415653, https://doi.org/10.1155/2014/415653.

[4] F.I. Islim, N. Saleem, T. Patankar, A Review and Journey in Intrasaccular Treatment of Intracranial Aneurysms, June 15, 2023, https://doi.org/10.1177/15910199231182460 (Published online).

[5] P. Texakalidis, K. Bekelis, E. Atallah, S. Tjoumakaris, R.H. Rosenwasser, P. Jabbour, Flow diversion with the pipeline embolization device for patients with intracranial aneurysms and antiplatelet therapy: a systematic literature review, Clin. Neurol. Neurosurg. 161 (2017) 78–87, https://doi.org/10.1016/J.CLINEURO.2017.08.003.

[6] S.P. Ferns, M.E.S. Sprengers, W.J. Van Rooij, et al., Coiling of intracranial aneurysms: a systematic review on initial occlusion and reopening and retreatment rates, Stroke 40 (8) (2009), https://doi.org/10.1161/STROKEAHA.109.553099/ASSET/7BDF6C3A-EA1D-41CF-8643-8EC89440E63F/ASSETS/GRAPHIC/2FF3.JPEG.

[7] K. Zhang, Z.L. Wang, B.L. Gao, et al., Use of a first large-sized coil versus conventional coils for embolization of cerebral aneurysms: effects on packing density, coil length, and durable occlusion, World Neurosurg. 127 (2019) e685–e691, https://doi.org/10.1016/J.WNEU.2019.03.242.

[8] Y. Hong, Y.J. Wang, Z. Deng, Q. Wu, J.M. Zhang, Stent-assisted coiling versus coiling in treatment of intracranial aneurysm: a systematic review and meta-analysis, PLoS One 9 (1) (2014) e82311, https://doi.org/10.1371/JOURNAL.PONE.0082311.

[9] B.K. Hendricks, J.S. Yoon, K. Yaeger, et al., Wide-neck aneurysms: systematic review of the neurosurgical literature with a focus on definition and clinical implications, J. Neurosurg. 133 (1) (2019) 159–165, https://doi.org/10.3171/2019.3.JNS183160.

[11] K. Fatania, T. Patankar, Comprehensive review of the recent advances in devices for endovascular treatment of complex brain aneurysms, Br. J. Radiol. 95 (1129) (2022), https://doi.org/10.1259/BJR.20210538.

[12] R. Pranata, E. Yonas, H. Deka, R. Vania, J. July, Stent-assisted coiling of intracranial aneurysms using a nitinol-based stent (Neuroform Atlas): a systematic review and meta-analysis, Cardiovasc. Intervent. Radiol. 43 (7) (2020) 1049–1061, https://doi.org/10.1007/S00270-020-02502-9/FIGURES/5.

[13] K. El Naamani, A. Syal, N.C. Field, et al., The Enterprise Stent…Still Useful After All These Years, December 28, 2023, https://doi.org/10.1177/15910199231224004 (Published online).

[14] A. Nania, N. Dobbs, J. Duplessis, P. Keston, J. Downer, Early experience treating intracranial aneurysms using Accero: a novel, fully visible, low profile braided stent with platinum–nitinol composite wire technology, J Neurointerv Surg. 13 (1) (2021) 49–53, https://doi.org/10.1136/NEURINTSURG-2020-015918.

[15] M.A. Pérez, H. Henkes, W. Kurre, et al., Results of the pToWin Study: using the pCONUS device for the treatment of wide-neck intracranial aneurysms, J. Clin. Med. 11 (3) (2022), https://doi.org/10.3390/JCM11030884.

[16] J. Raymond, F. Guilbert, D. Roy, Neck-bridge device for endovascular treatment of wide-neck bifurcation aneurysms: initial experience 221 (2) (2001) 318–326, https://doi.org/10.1148/RADIOL.2212010474.

[17] A. Sirakov, P. Bhogal, K. Sirakova, et al., Endovascular treatment of wide-necked intracranial aneurysms using the Nautilus Intrasaccular System: initial case series of 41 patients at a single center, J Neurointerv Surg. 15 (10) (2023) 989–994, https://doi.org/10.1136/JNIS-2022-019295.

[18] R. Raj, J. Numminen, Initial experiences with the Trenza embolization device for the treatment of wide-neck intracranial aneurysms: a 12-patient case series, Am. J. Neuroradiol. 45 (4) (2024) 418–423, https://doi.org/10.3174/AJNR.A8153.

[19] T. Liebig, G. Gal, C. O'Kelly, et al., Neqstent coil-assisted flow diverter (NQS) for the treatment of bifurcation aneurysms: the coil-assisted flow diversion safety and performance study (CAFI), J Neurointerv Surg. 16 (7) (2024) 721–725, https://doi.org/10.1136/JNIS-2022-020056.

[20] T. Gunnarsson, L. Da Costa, M.P.S. Souza, W. Montanera, T.R. Marotta, Guidewire tip detachment during stent-assisted coiling of an intracranial aneurysm. A case report, Interv. Neuroradiol. 15 (1) (2009) 93–98, https://doi.org/10.1177/159101990901500115.

[21] T. Liebig, M. Killer-Oberpfalzer, G. Gal, et al., The safety and effectiveness of the contour neurovascular system (contour) for the treatment of bifurcation aneurysms: the CERUS study, Neurosurgery 90 (3) (2022) 270–277, https://doi.org/10.1227/NEU.0000000000001783.

[22] D. Fiorella, A. Molyneux, A. Coon, et al., Safety and effectiveness of the Woven EndoBridge (WEB) system for the treatment of wide necked bifurcation aneurysms: final 5 year results of the pivotal WEB Intra-saccular Therapy study (WEB-IT), J Neurointerv Surg. 15 (12) (2023) 1175–1180, https://doi.org/10.1136/JNIS-2023-020611.

[23] F. Wodarg, Y. Ozpeynirci, J. Hensler, O. Jansen, T. Liebig, Contour-Assisted coiling with jailed microcatheter May result in better occlusion (CoCoJaMBO) in wide-necked intracranial aneurysms: proof of principle and immediate angiographic results, Interv. Neuroradiol. 29 (1) (2023) 79–87, https://doi.org/10.1177/15910199211069782.

[24] F. Gallo-Pineda, M. Fernáandez-Góomez, C. Hidalgo-Barranco, Rescue stenting after artery occlusion as a complication of an intrasaccular device–assisted coiling embolization: illustrative case, J Neurosurg Case Lessons. 5 (26) (2023), https://doi.org/10.3171/CASE23171.

[25] C. Bechtold, R. Lima de Miranda, E. Quandt, Capability of sputtered micro-patterned NiTi thick films, Shape Mem Superelasticity. 1 (3) (2015) 286–293, https://doi.org/10.1007/S40830-015-0029-9/FIGURES/8.

[26] L. Petrini, F. Migliavacca, S. Gialanella, Biomedical applications of shape memory alloys, J Metall. 2011 (1) (2011) 501483, https://doi.org/10.1155/2011/501483.

[27] D. Stoeckel, A. Pelton, T. Duerig, Self-expanding Nitinol stents: material and design considerations, Eur. Radiol. 14 (2) (2004) 292–301, https://doi.org/10.1007/S00330-003-2022-5/FIGURES/22.

[28] T.W. Duerig, M. Wholey, A comparison of balloon- and self-expanding stents, Minim. Invasive Ther. Allied Technol. 11 (4) (2002) 173–178, https://doi.org/10.1080/136457002760273386.

[29] M.J. Vansteensel, E.G.M. Pels, M.G. Bleichner, et al., Fully implanted brain–computer interface in a locked-in patient with ALS, N. Engl. J. Med. 375 (21) (2016) 2060–2066, https://doi.org/10.1056/NEJMOA1608085/SUPPL_FILE/NEJMOA1608085_DISCLOSURES.PDF.

[31] C. Bechtold, R. Lima de Miranda, C. Chluba, C. Zamponi, E. Quandt, Method for fabricating miniaturized NiTi self-expandable thin film devices with increased radiopacity, Shape Mem Superelasticity. 2 (4) (2016) 391–398, https://doi.org/10.1007/S40830-016-0086-8/FIGURES/6.

[32] C. Chluba, K. Siemsen, C. Bechtold, et al., Microfabricated bioelectrodes on self-expandable NiTi thin film devices for implants and diagnostic instruments, Biosens. Bioelectron. 153 (2020) 112034, https://doi.org/10.1016/J.BIOS.2020.112034.

[33] P. Velvaluri, M.S. Pravdivtseva, P. Berg, et al., Thin-film patient-specific flow diverter stents for the treatment of intracranial aneurysms, Adv Mater Technol. 6 (9) (2021) 2100384, https://doi.org/10.1002/ADMT.202100384.

[34] P. Velvaluri, A. Soor, P. Plucinsky, R.L. de Miranda, R.D. James, E. Quandt, Origami-inspired thin-film shape memory alloy devices, Sci. Report. 11 (1) (2021) 1–10, https://doi.org/10.1038/s41598-021-90217-3.

[35] T. Motsenbocker, E. Goff, Radial Expansion Force Measurement Technology. EP1703830A2, November 10, 2004 (Published online).

[36] M.S. Pravdivtseva, A.N. Pravdivtsev, S. Peters, et al., The effect of the size of the new contour neurovascular device for altering intraaneurysmal flow, Interv. Neuroradiol. (2023), https://doi.org/10.1177/15910199221145985 (Published online).

[37] L. Zarrinkoob, K. Ambarki, A. Wåhlin, R. Birgander, A. Eklund, J. Malm, Blood flow distribution in cerebral arteries, J. Cereb. Blood Flow Metab. 35 (4) (2015) 648, https://doi.org/10.1038/JCBFM.2014.241.

[38] C. Sadasivan, R. Dholakia, L. Peeling, et al., Angiographic assessment of the efficacy of flow diverter treatment for cerebral aneurysms 25 (6) (2019) 655–663, https://doi.org/10.1177/1591019919860829.

[39] C. Sadasivan, B.B. Lieber, M.J. Gounis, D.K. Lopes, L.N. Hopkins, Angiographic quantification of contrast medium washout from cerebral aneurysms after stent placement, AJNR Am. J. Neuroradiol. 23 (7) (2002) 1214. https://pmc.ncbi.nlm.nih.gov/articles/PMC8185722/. (Accessed 2 December 2024).

[40] S. Srivastava, Roekel D. Van, J.L. Wright, M. Bruce, M. Dighe, Contrast-enhanced ultrasound (CEUS) in the evaluation of bladder pathologies: review, WFUMB Ultrasound Open. 1 (2) (2023) 100019, https://doi.org/10.1016/J.WFUMBO.2023.100019.

[41] C. Sadasivan, L. Cesar, J. Seong, A.K. Wakhloo, B.B. Lieber, Treatment of rabbit elastase-induced aneurysm models by flow diverters: development of quantifiable indexes of device performance using digital subtraction angiography, IEEE Trans. Med. Imaging 28 (7) (2009) 1117–1125, https://doi.org/10.1109/TMI.2008.2012162.

[42] Sela Medical, Neqstent™ Coil Assisted Flow Diverter: Sizing and Applications, 2024 (Brochure).

[44] M.S. Pravdivtseva, Python Script for Post-processing Angiographic Contrast Time Density Curves, 2022, https://doi.org/10.5281/ZENODO.7447570 (Published online).

[45] N. Goyal, D. Hoit, J. Dinitto, et al., How to WEB: a practical review of methodology for the use of the Woven EndoBridge, J Neurointerv Surg. 12 (5) (2020) 512–520, https://doi.org/10.1136/NEURINTSURG-2019-015506.

[46] G. Bellanger, J. Darcourt, A.C. Januel, C. Cognard, The reversed umbrella: displacement of a Contour device into an MCA aneurysm 18 months after treatment, J Neurointerv Surg. 16 (2) (2024) 213–215, https://doi.org/10.1136/JNIS-2022-019814.

[47] S. Lukic, S. Jankovic, K.S. Popovic, D. Bankovic, P. Popovic, M. Mijailovic, Analysis of risk factors for perifocal oedema after endovascular embolization of unruptured intracranial arterial aneurysms, Radiol. Oncol. 49 (4) (2015) 341, https://doi.org/10.1515/RAON-2015-0044.

[48] O. Mansour, M. Khalil, J. Weber, M. Schumacher, Light aneurismal coiling with satisfactory obliteration on follow up, a case report, is it a matter of full compaction or flow dynamic changes? Internet J Interv Med. 1 (1) (2009) https://doi.org/10.5580/19CA.

[49] Ö. Krischek, E. Miloslavski, S. Fischer, S. Shrivastava, H. Henkes, A comparison of functional and physical properties of self-expanding intracranial stents [Neuroform3, Wingspan, Solitaire, Leo(+), Enterprise], Minim. Invasive Neurosurg. 54 (1) (2011) 21–28, https://doi.org/10.1055/S-0031-1271681/BIB.

[50] P. Velvaluri, M.S. Pravdivtseva, J. Hensler, et al., A realistic way to investigate the design, and mechanical properties of flow diverter stents, Expert Rev. Med. Devices 18 (6) (2021) 569–579, https://doi.org/10.1080/17434440.2021.1920923.

[51] S. Cho, W. Jo, Y. Jo, K.H. Yang, J.C. Park, D.H. Lee, Bench-top comparison of physical properties of 4 commercially-available self-expanding intracranial stents,

Neurointervention 12 (1) (2017) 31–39, https://doi.org/10.5469/NEUROINT.2017.12.1.31.
[52] G. Siekmeyer, A. Schüßler, R.L. De Miranda, E. Quandt, Comparison of the fatigue performance of commercially produced nitinol samples versus sputter-deposited nitinol, J. Mater. Eng. Perform. 23 (7) (2014) 2437–2445, https://doi.org/10.1007/S11665-014-1101-X/FIGURES/11.
[53] R. Rebelo, N. Vila, R. Fangueiro, S. Carvalho, S. Rana, Influence of design parameters on the mechanical behavior and porosity of braided fibrous stents, Mater. Des. 86 (2015) 237–247, https://doi.org/10.1016/J.MATDES.2015.07.051.
[54] J.H. Kim, T.J. Kang, W.R. Yu, Mechanical modeling of self-expandable stent fabricated using braiding technology, J. Biomech. 41 (15) (2008) 3202–3212, https://doi.org/10.1016/J.JBIOMECH.2008.08.005.
[55] B. Mine, L. Pierot, B. Lubicz, Intrasaccular flow-diversion for treatment of intracranial aneurysms: the Woven EndoBridge, Expert Rev. Med. Devices 11 (3) (2014) 315–325, https://doi.org/10.1586/17434440.2014.907741.
[56] U. Kutbay, O. Algin, Quantitative Radial Force Measurements of Woven EndoBridge Devices, October 31, 2023, https://doi.org/10.1177/15910199231209072 (Published online).
[57] J. Korte, F. Gaidzik, N. Larsen, et al., In vitro and in silico assessment of flow modulation after deploying the Contour Neurovascular System in intracranial aneurysm models, J Neurointerv Surg. 16 (8) (2024) 815–823, https://doi.org/10.1136/JNIS-2023-020403.
[58] C. Roloff, D. Stucht, O. Beuing, P. Berg, Comparison of intracranial aneurysm flow quantification techniques: standard PIV vs stereoscopic PIV vs tomographic PIV vs phase-contrast MRI vs CFD, J Neurointerv Surg. 11 (3) (2019) 275–282, https://doi.org/10.1136/NEURINTSURG-2018-013921.
[59] S. Kim, H. Yang, J.H. Oh, Y.B. Kim, Quantitative analysis of hemodynamic changes induced by the discrepancy between the sizes of the flow diverter and parent artery, Sci. Report. 14 (1) (2024) 1–8, https://doi.org/10.1038/s41598-024-61312-y.
[60] M.S. Pravdivtseva, E. Peschke, T. Lindner, et al., 3D-printed, patient-specific intracranial aneurysm models: from clinical data to flow experiments with endovascular devices, Med. Phys. 48 (4) (2021) 1469–1484, https://doi.org/10.1002/MP.14714.
[61] S. Sindeev, P.G. Arnold, S. Frolov, et al., Phase-contrast MRI versus numerical simulation to quantify hemodynamical changes in cerebral aneurysms after flow diverter treatment, PLoS One 13 (1) (2018) e0190696, https://doi.org/10.1371/JOURNAL.PONE.0190696.
[62] F. Gallo-Pineda, M. Fernández-Gómez, C. Domínguez-Rodríguez, et al., Evaluating efficacy and complications of contour intrasaccular device in cerebral aneurysm management: a multicenter analysis, World Neurosurg. 183 (2024) e738–e746, https://doi.org/10.1016/J.WNEU.2024.01.017.